Nanoscale

PAPER

View Article Online
View Journal | View Issue

Cite this: *Nanoscale*, 2025, **17**, 3900

Strain-tunable optoelectronic and photocatalytic properties of 2D GaN/$MoSi_2P_4$ heterobilayers: potential optoelectronic/photocatalytic materials†

Huabing Shu, *[a] Feifan Wang,[b] Kai Ren *[c] and Jiyuan Guo [a]

Received 31st October 2024,
Accepted 16th December 2024

DOI: 10.1039/d4nr04545a

rsc.li/nanoscale

Herein, we propose a new GaN/$MoSi_2P_4$ van der Waals (vdWs) heterostructure constructed by vertically stacking GaN and $MoSi_2P_4$ monolayers. Its electronic, optical, and photocatalytic properties are explored *via* DFT+G_0W_0+BSE calculations. The calculated binding energy and phonon spectrum demonstrated the material's high stabilities. The projected band structure of GaN/$MoSi_2P_4$ suggests that it has a desirable direct bandgap and displays type-I band alignment. It also exhibits a particularly large absorption coefficient for visible and near-infrared light while considering electron–hole interactions. Intriguingly, a small biaxial tensile strain of +1% can transform the band alignment to type-II using a direct Z-scheme mechanism for water splitting. The Z-scheme optimizes redox ability, thus perfectly engulfing the redox potentials of water and showing excellent photocatalytic activity in different layers. Our findings indicate that the GaN/$MoSi_2P_4$ vdWs heterostructure is a promising optoelectronic and photocatalytic material.

1 Introduction

Two-dimensional (2D) materials have attracted tremendous interest owing to their novel properties and promising applications in electronics and optoelectronics.[1–3] For a single 2D material, there exists a limitation in photocatalytic, photovoltaic, and optoelectronic devices owing to the swift recombination of photoexcited charge carriers. The vertical stacking of diverse 2D materials facilitates the fabrication of van der Waals (vdWs) heterostructures, which have been achieved experimentally, such as graphene/MoS_2,[4] $MoSe_2$/MoS_2,[5] and h-BN/WS_2.[6] At present, vdWs engineering has been regarded as the most feasible way to integrate the intrinsic properties of two pristine 2D materials.[7–9] More importantly, semiconducting vdWs heterostructures can offer a large active junction area to absorb more photons and induce more exciton states, thus leading to enhanced light absorption and photocurrent. In such vdWs heterostructures, type-II band alignment at interfaces is especially preferred owing to effective space segregation of photoexcited electrons and holes, consequently suppressing the recombination of electron–hole (e–h) pairs. In addition, type-II vdWs heterostructures with the Z-scheme can optimize redox ability through interface electron–hole recombination and facilitate the hydrogen evolution reaction (HER) and oxygen evolution reaction (OER),[10] thereby ensuring the photocatalytic activity of the vdWs heterostructure. As a result, the design and exploration of new 2D vdWs heterostructures are highly necessary for photocatalytic, photovoltaic, and optoelectronic devices.

Very recently, a novel 2D $MoSi_2N_4$ monolayer has been successfully synthesized by employing chemical vapor deposition, which displayed excellent environmental stability, a high strength of ~66 GP, a moderate indirect bandgap of ~1.94 eV, and a high hole (electron) mobility of ~1200 (270) $cm^2\ V^{-1}\ s^{-1}$.[11] P and N atoms belong to the same main group and possess the same number of valence electrons. A $MoSi_2P_4$ monolayer has also been demonstrated to be dynamically and thermally stable[12] and exhibits a direct bandgap of ~1.32 eV at the HSE06 level. The predicted hole (electron) mobility can achieve a large value of ~1429 (258) $cm^2\ V^{-1}\ s^{-1}$,[13] which is significantly larger than those (hole: 200 $cm^2\ V^{-1}\ s^{-1}$; electron: 72 $cm^2\ V^{-1}\ s^{-1}$)[14] of monolayer MoS_2. A $MoSi_2P_4$ monolayer with a direct gap also shows a tunable electronic property under a wide strain range and an outstanding absorption of visible light.[13,15] However, monolayer gallium nitride (GaN) has also been synthesized by applying graphene-encapsulated growth technique and sonochemical exfoliation.[16,17] The GaN monolayer is a wide indirect semiconductor with a bandgap of ~4.44 eV (ref. 18) and high carrier mobility of ~10^3 $cm^2\ V^{-1}\ s^{-1}$,[19] leading to the prominent absorption of near-ultraviolet

[a]School of Science, Jiangsu University of Science and Technology, Zhenjiang 212001, China. E-mail: shuhuabing@just.edu.cn
[b]Jiangsu Co-Innovation Centre of Efficient Processing and Utilization of Forest Resources, College of Chemical Engineering, Nanjing Forestry University, Nanjing 210037, China
[c]School of Mechanical and Electronic Engineering, Nanjing Forestry University, Nanjing 210037, China. E-mail: kairen@njfu.edu.cn

† Electronic supplementary information (ESI) available. See DOI: https://doi.org/10.1039/d4nr04545a

light. The electronic and optical properties of 2D GaN can be broadly modulated under external strain.[18] Some theoretical reports have also pointed out that monolayer GaN can form a type-II heterostructure with other monolayer MX_2 (such as WS_2, WSe_2, and MoS_2).[20,21] These suggest that GaN and $MoSi_2P_4$ monolayers have potential applications in electronic and optoelectronic devices.

Because $MoSi_2P_4$ and GaN monolayers are both semiconductors with the same hexagonal structure and similar lattice parameters ($MoSi_2P_4$: 3.46 Å;[22] GaN: 3.20 Å (ref. 18)), a GaN/$MoSi_2P_4$ vdWs heterobilayer stacked vertically by GaN and $MoSi_2P_4$ monolayers is proposed, and the following questions arise immediately: (1) Can a GaN monolayer be stacked on a $MoSi_2P_4$ monolayer to form structurally stable vdWs heterostructures? (2) What are the electronic and optical characteristics of such vdWs heterostructures? (3) Can such vdWs heterostructures be used in device design? To answer these questions, this study employs first-principles calculations to investigate GaN/$MoSi_2P_4$ vdWs heterobilayer with six stacking configurations. The structural, electronic, photocatalytic, and optical properties of the GaN/$MoSi_2P_4$ with AA5 stacking mode are investigated systemically owing to their relatively high stabilities. AA5 GaN/$MoSi_2P_4$ displays type-I band alignment, which is unfavorable for separating photoexcited e–h pairs. Its optical spectrum shows desirable absorption from the near-infrared to the visible range. Notably, band alignment can be modulated by the application of in-plane biaxial strains. Specifically, the transition from type-I to type-II band alignment can be achieved by introducing a small tensile strain. Our results point out the potential of the AA5 GaN/$MoSi_2P_4$ heterobilayer as a novel strain-tunable optoelectronic and photocatalytic material.

2 Computational details and methods

All the ground-state calculations were performed using Quantum ESPRESSO code.[23] A vacuum thickness of 23 Å in the direction perpendicular to the surface was adopted to reduce the coupling between the two adjacent layers. Perdew–Burke–Ernzerhof (PBE) functional[24] was used to optimize the structures of the observed systems. We used the vdW-DF method to describe the weak interlayer coupling,[25] and an energy cutoff of 952 eV was utilized for the plane wave expansion. The convergence thresholds for force and energy were established at 10^{-2} eV and 10^{-5} eV Å^{-1}, respectively. The Brillouin zone was sampled using a k-point mesh with dimensions of 18 × 18 × 1. The phonon band structure was computed using the density functional perturbation theory,[26] and the acoustic sum rule was used for the vibrational frequencies of the Γ point. To examine the thermal stability, *ab initio* molecular dynamics (AIMD) simulations were executed, in which a 4 × 4 × 1 supercell was adopted at 400 K and dynamics simulations lasted for 10 ps (a time step of 1 fs). The Nosé algorithm was employed to control the temperature in the NVT ensemble.

The free energy change (ΔG) during the hydrogen reduction and water oxidation reactions was calculated utilizing the method developed by Nørskov *et al.*[27,28] The ΔG of an electrochemical reaction can be obtained by applying the following equation:

$$\Delta G = \Delta E + \Delta E_{zpe} - T\Delta S + \Delta G_{pH} + \Delta G_U, \quad (1)$$

where ΔE is the total energy difference between the adsorption and desorption states and T denotes the system temperature at 298.15 K. The zero-point energy differential (ΔE_{zpe}) and entropy differential (ΔS) quantify the disparities between the adsorbed state and gaseous phase, respectively. In each system, E_{zpe} is determined by calculating the sum of vibrational frequencies across all normal modes ν, expressed as $E_{zpe} = 1/2\sum h\nu$. The entropies for the free O_2, H_2, and H_2O molecules are derived from the NIST database.[29] The equation $\Delta G_{pH} = 0.059 \times pH$ represents the free-energy contribution at varying pH values. The influence of a potential bias is accounted for in all states involving a single electron or hole within the electrode by applying an energy shift of $\Delta G_U = -eU$, where U denotes the electrode potential in relation to the standard hydrogen electrode. Under standard conditions (pH = 0, U = 0), the free energy of a proton–electron pair ($H^+ + e^-$) is equated to $1/2G_{H_2}$. The free energy of O_2 comes from $G_{O_2} = 2G_{H_2O} - 2G_{H_2} - 4.920$ eV. This is because triplet ground state O_2 calculated by the density-functional theory (DFT) is poorly described.

The quasi-particle (QP) energies were obtained by applying the G_0W_0 method along with plasmon-pole approximation.[30,31] We used 982 unoccupied bands, 70 Ry cutoff energy for the dielectric matrix, response cutoffs of 12 Ry, and box-shaped truncation of 30 a.u. to obtain the converged dielectric function, where the convergence of the QP bandgap was within 50 meV. The excitonic effects have been included with a fine k-point grid of 36 × 36 × 1 by solving the Bethe-Salpeter equation (BSE):[32,33]

$$(E^{QP}_{c\mathbf{k}} - E^{QP}_{v\mathbf{k}})A^S_{vc\mathbf{k}} + \sum_{\mathbf{k}'v'c'} \langle vc\mathbf{k}|K^{eh}|v'c'\mathbf{k}'\rangle A^S_{v'c'\mathbf{k}'} = \Omega^S A^S_{vc\mathbf{k}}, \quad (2)$$

where $E^{QP}_{v\mathbf{k}}/E^{QP}_{c\mathbf{k}}$ is the QP energies for the valence/conduction band states, Ω^S is the excitation energy, $A^S_{vc\mathbf{k}}$ is the exciton amplitude, and K^{eh} is the e–h coupling kernel. All occupied bands and 17 unoccupied bands were used to construct the e–h coupling kernel. Due to the depolarization effects of the two-dimensional material,[34] only the polarized light parallel to the surface was used to calculate the optical properties of the observed system. The G_0W_0+BSE calculations were performed using the YAMBO code.[35]

3 Results and discussion

3.1 Structure and electronic properties

The isolated GaN and $MoSi_2P_4$ monolayers are first investigated by their crystals and band structures, as shown in Fig. S1 of ESI.† The optimized lattice constants (a/b) for the hexagonal

GaN and $MoSi_2P_4$ monolayers are 3.201 Å and 3.468 Å, respectively. The $MoSi_2P_4$ monolayer is predicted to have a direct bandgap of about 0.685 eV by applying the PBE method, which is further increased to 1.335 eV using the G_0W_0 method (as shown in Fig. S2†). These calculation results align well with previously reported theoretical predictions.[36–39] The calculated phonon dispersions of GaN and $MoSi_2P_4$ monolayers can be found in Fig. S3 of the ESI,† in which they are suggested to be dynamically stable owing to no negative phonon frequency. Previously, their thermal stabilities were verified at a high temperature of 1000 K for GaN monolayer[40] (700 K for $MoSi_2P_4$ monolayer[41]).

Next, six possible high-symmetry stacking patterns are considered AA1–AA6 configurations, and their optimized structures are depicted in Fig. 1. These stacking configurations have been estimated by their binding energies (E_b), which can judge their energetic stabilities, thus pointing out the feasibility of experimental preparation. The binding energy can be calculated using the following equation: $E_b = (E_{GaN/MoSi_2P_4} - E_{GaN} - E_{MoSi_2P_4})/S$, where $E_{GaN/MoSi_2P_4}$, E_{GaN}, and $E_{MoSi_2P_4}$ are total energies of $GaN/MoSi_2P_4$ heterobilayer, GaN monolayer, and $MoSi_2P_4$ monolayer, respectively. S is the interface area of the $GaN/MoSi_2P_4$ heterobilayer. The obtained E_b values are presented in Fig. 2a, in which the E_b values are all negative and limited in the energy range of −12 to −18 meV Å^{-2}. The estimated binding energies of $GaN/MoSi_2P_4$ heterobilayers are comparable to those (−15 to −20 meV Å^{-2}) of typical vdWs layered materials,[42] indicating that the interlayer interaction between GaN and $MoSi_2P_4$ layers belongs to the vdWs force. In particular, the AA5 configuration with a lattice constant of 3.407 Å and an interlayer distance of 3.429 Å provides the lowest binding energy of approximately −17 meV Å^{-2}, suggesting that it is the most favorable energetically and can be fabricated experimentally. Fig. 2b shows the phonon spectra of the AA5 configuration, in which no imaginary frequency is found, suggesting its dynamical stability. In addition, the thermal stability of AA5 $GaN/MoSi_2P_4$ is confirmed by the AIMD simulations, as depicted in Fig. 3. It can

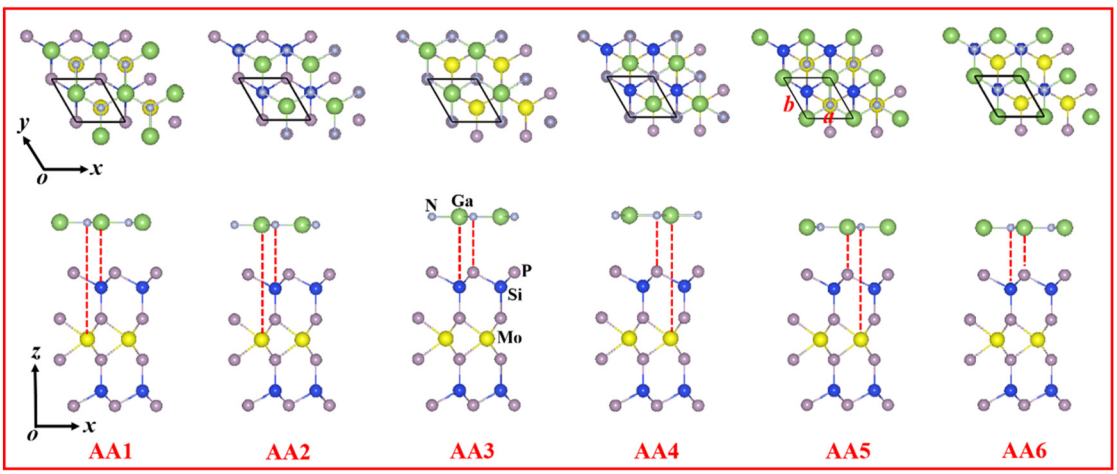

Fig. 1 Top and side views of optimized configurations for $GaN/MoSi_2P_4$ heterobilayers with six stacking patterns.

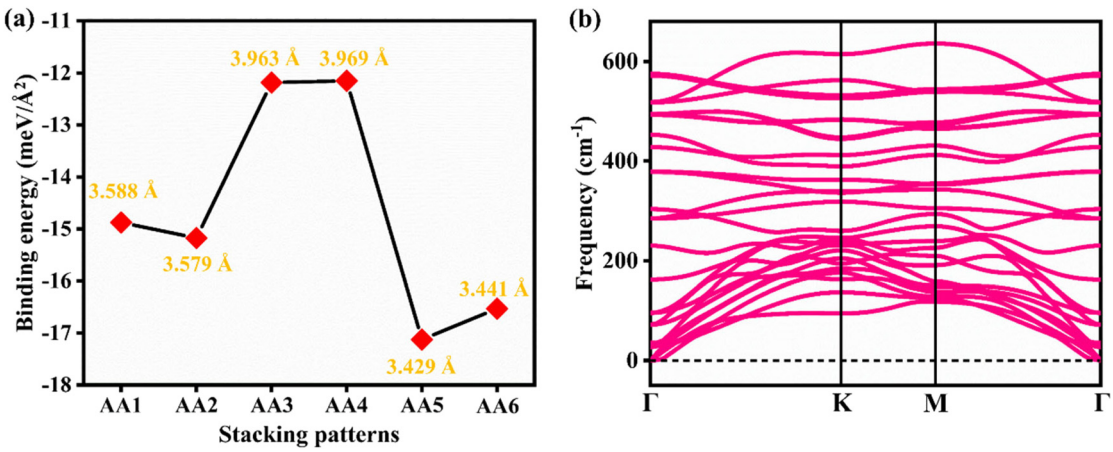

Fig. 2 (a) Computed binding energies of $GaN/MoSi_2P_4$ heterosbilayers with six stacking patterns. The interlayer distances of the heterobilayer are marked by orange. (b) Phonon spectrum of the AA5 $GaN/MoSi_2P_4$ heterosbilayer.

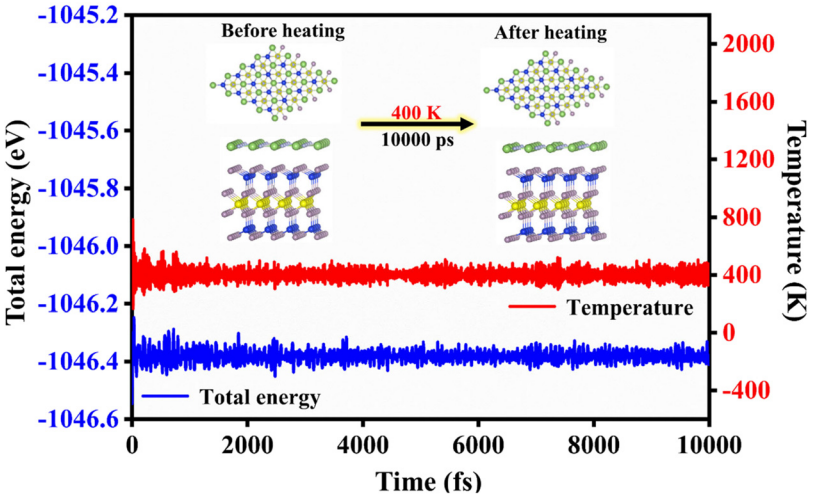

Fig. 3 Variable total energy and temperature of the AA5 GaN/$MoSi_2P_4$ heterosbilayer during *ab initio* molecular dynamics heating 10 000 fs at 400 K.

be found that the structure is intact at a temperature of 400 K. Therefore, the subsequent discussions are mainly focused on GaN/$MoSi_2P_4$ heterobilayer with AA5 configuration.

For GaN/$MoSi_2P_4$ heterobilayer with AA5 configuration, the projected band structure obtained by the PBE method is shown in Fig. 4a. It can be found that the band structure of every monolayer is retained perfectly, further implying that the interface of the heterostructure is supported by the weak vdWs interaction. Additionally, AA5 exhibits a direct bandgap of about 0.825 eV at the PBE level, which shows that the bandgap (0.685 eV) of the isolated $MoSi_2P_4$ monolayer can be improved by forming the vdWs heterobilayer. The valence band maximum (VBM) and conduction band minimum (CBM) of the AA5 GaN/$MoSi_2P_4$ heterobilayer are at the K point, identical to the isolated $MoSi_2P_4$ monolayer. Fig. 4a shows that both the VBM and CBM originate from the $MoSi_2P_4$ layer, which is further verified by the calculated partial charge distributions for the VBM and CBM (see the insets in Fig. 4b). This suggests that the AA5 configuration is a typical type-I vdWs heterostructure, which makes it suitable for light-emitting applications. Additionally, the differential charge density along the *c* direction is calculated, as shown in Fig. S4,† where the accumulated and depleted electrons are suggested *via* yellow and cyan, respectively. It can be found that the electron is gathered near the $MoSi_2P_4$ layer, while the GaN layer loses the electron.

In addition, the spin–orbit coupling effects on the band structure of the AA5 configuration are checked owing to the heavier Mo atom, as shown in Fig. S5.† The bandgap decreases to 0.741 eV at the PBE level, which is attributed to the spin splitting of the VBM at the K point. The spin splitting Δ_{soc} of the VBM is approximately 87 meV, while that of the CBM is only 4 meV. Previously, the MoS_2 monolayer has illustrated that the Δ_{soc} of the VBM is 146 meV.[43] The spin splitting of the VBM from the Mo atom can induce the splitting of the lowest-energy peak in the optical absorption spectrum; however, they do not influence the whole optical absorption of the MoS_2

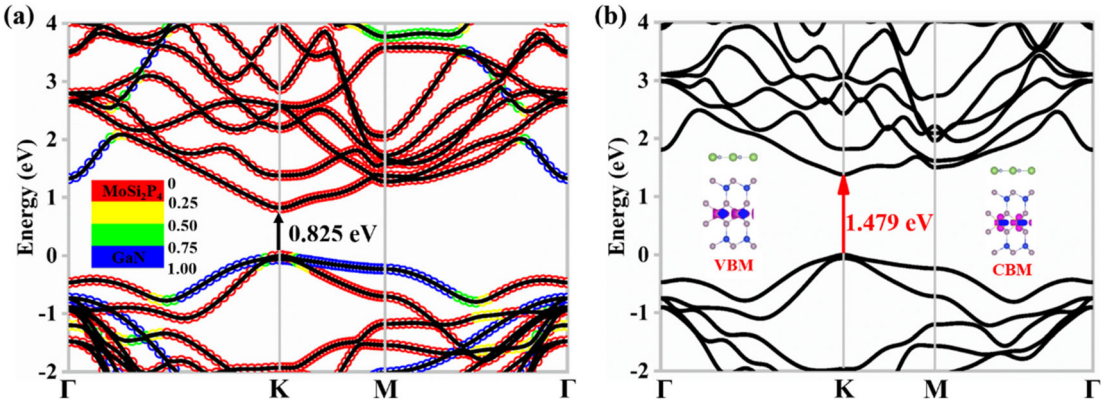

Fig. 4 (a) Projected and (b) quasi-particle band structures of the AA5 GaN/$MoSi_2P_4$ heterobilayer at the PBE and G_0W_0 methods, respectively. Isosurface values for the VBM and CBM are set to 5×10^{-3} e $Å^{-3}$, and the color pink shows the distribution.

monolayer.[43,44] Therefore, the spin–orbit coupling effects are not included in the following calculations. We also calculated the quasi-particle (QP) band structure of the AA5 configuration by applying the G_0W_0 method (Fig. 4b), in which the band structure is acceptable considering only electron–electron interactions. Under the G_0W_0 approximation, the PBE bandgap of 0.825 eV is corrected to 1.479 eV. The more accurate quasi-particle bandgap of 1.479 eV together with its direct nature indicates that the AA5 GaN/$MoSi_2P_4$ heterobilayer has potential in optoelectronic applications.

In addition, it is noteworthy that the two highest valence bands at the K point are very close and the second valence band originates from the GaN layer (Fig. 4a). There is only an energy difference of 63 meV between the two valence bands, suggesting that the two valence bands compete under an external factor, such as in-plane strain. In the experiment, the in-plane tensile strain on the 2D materials can be achieved easily compared to the in-plane compressive strain.[45,46] Thus, we explore only the effects of biaxial tensile strain on the valence band edge of the AA5 configuration. The calculated quasi-particle band structures of the AA5 configuration under different biaxial tensile strains (δ) are provided in Fig. 5a–c. As the applied tensile strain increases, the valence band edge changes. When the δ is increased to +1%, the GaN and $MoSi_2P_4$ layers contribute to the VBM and CBM, respectively, as shown in the inset of Fig. 5a. This illustrates that the band alignment in the AA5 GaN/$MoSi_2P_4$ heterobilayer is transformed from type-I to type-II at δ = +1%. Additionally, the type-II band alignment and direct nature of the bandgap can be retained within the examined strain range from +1% to +5% for AA5 GaN/$MoSi_2P_4$. The predicted quasi-particle bandgap decreases linearly from 1.325 eV (δ = +1%) to 0.751 eV (δ = +5%) with the increased tensile strains. Although the PBE method underestimates the bandgap of the AA5 GaN/$MoSi_2P_4$, the changing trend in the bandgap seems to be the same as the G_0W_0 method in the observed strain range of 0–+5% (Fig. 5d). In addition, the phonon dispersions of AA5 GaN/$MoSi_2P_4$ at +5% tensile strain are calculated, and the calculated results are shown in Fig. S6.† No negative frequency is found, suggesting that the strained structure is still stable dynamically.

The formed type-II heterostructure usually conforms to the double-transfer mode or the Z-scheme mode under illumination, as illustrated in Fig. S7 of the ESI.† To confirm the mode in the strained GaN/$MoSi_2P_4$, we perform a Bader's charge calculation in AA5 GaN/$MoSi_2P_4$. The calculation result shows

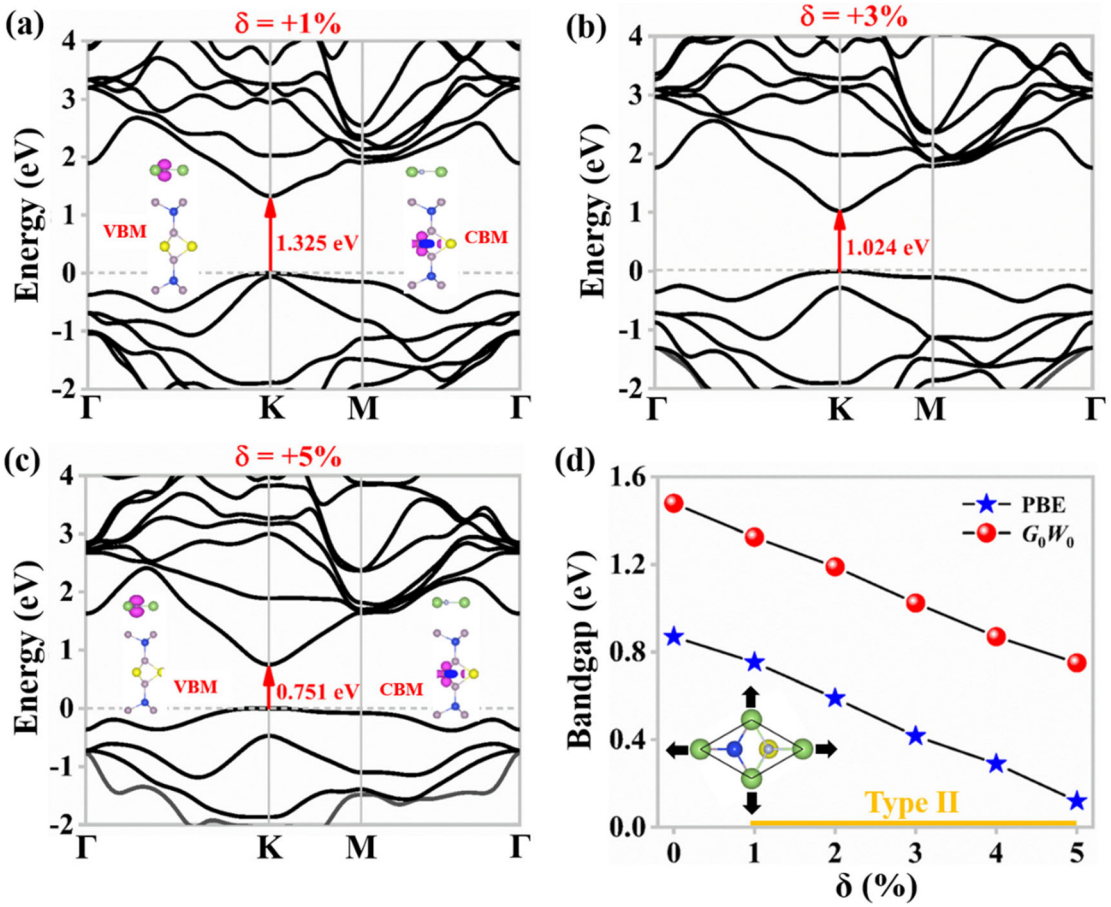

Fig. 5 (a)–(c) Quasi-particle band structures and (d) variable bandgaps of the AA5 GaN/$MoSi_2P_4$ heterostructure under biaxial tensile strains (δ). Isosurface values for the VBM and CBM are set to 5×10^{-3} e Å^{-3}.

that the electron of about $9.07 \times 10^{-3}e$ near the interface is transferred from the GaN layer to the $MoSi_2P_4$ layer at a biaxial tensile strain of +1%, which is less than $1.12 \times 10^{-2}e$ of the pristine structure. The direction of charge transfer is unchanged in the observed strain range of 0–+5%, and the transferred charge is reduced to $8.53 \times 10^{-3}e$ (+5%). In fact, the electron transfer at the interface leaves some holes at the GaN layer, causing an electric polarized field (E_1). The direction of the E_1 is pointed from the GaN layer to the $MoSi_2P_4$ layer. Once the light illuminates the AA5 heterobilayer, the electric polarized field induced by the charge transfer can hold back the transfers of the photogenerated electrons of the GaN layer and the hole of the $MoSi_2P_4$ layer by the reverse electric field force. However, this can increase the interface e–h recombination between the photogenerated electron from the $MoSi_2P_4$ layer and the photogenerated hole from the GaN layer, which should be attributed to the short electron-migration distance between the GaN and $MoSi_2P_4$ layers, thus forming a direct Z-scheme in the strained AA5 GaN/$MoSi_2P_4$ heterobilayer. Here, we show only the Z-scheme GaN/$MoSi_2P_4$ at the biaxial tensile strain of +1% due to the similar case at other observed strains, as shown in Fig. 6, in which the transfer processes of photogenerated electrons and holes can be understood clearly under the illumination.

It is also found that the interlayer bandgaps of the Z-scheme AA5 GaN/$MoSi_2P_4$ under different tensile strains are all smaller than the intralayer bandgaps in the GaN and $MoSi_2P_4$ layers, as illustrated in Fig. S8 of the ESI.† With increased tensile strains, the interlayer bandgap is greatly reduced from 1.325 eV (δ = 0) to 0.751 (δ = +5%). This indicates that the interlayer e–h recombination is much faster than that of the intralayer with the increased strains. When interlayer e–h recombination occurs, the excess electrons and holes can gather on the CBM of the GaN layer and VBM of the $MoSi_2P_4$ layer, respectively. This direct Z-scheme in AA5 GaN/$MoSi_2P_4$ is formed by a more positive potential of the VBM and a more negative potential of the CBM, achieving a strong oxidation and reduction ability. Taking the vacuum level as a reference, the predicted CBM of the GaN layer and the VBM of the $MoSi_2P_4$ layer in the strained systems are located at about −4.024/−3.856/−3.824 eV and −5.977/−5.949/−5.920 eV for the +1%/+3%/+5% tensile strain, respectively. In particular, the case of +1% is depicted in Fig. 6. Two band edges under the observed tensile strains can well straddle the redox potentials of water at pH = 0 (reduction/oxidation potential: −4.440/−5.670 eV), satisfying the thermodynamic conditions for overall water splitting. The pH-dependent water redox potentials (−4.440 + 0.059 × pH; −5.670 + 0.059 × pH)[47,48] yield a reduction/oxidation potential of −4.027/−5.257 eV at pH = 7, indicating that the AA5 GaN/$MoSi_2P_4$ heterobilayer in the strain range of +1%–+5% can also act as a water-splitting photocatalyst in a neutral environment.

In photocatalytic water splitting, the magnitude of the external potentials generated by photoexcited carriers directly dictates whether the half-reactions for water splitting can proceed spontaneously. The external potential (U_e) for the hydrogen reduction reaction *via* photoexcited electrons is identified as 0.416/0.584/0.616 V for the +1%/+3%/+5% biaxial tensile strain at pH = 0. The energy disparity between the CBM of GaN and the hydrogen reduction potential serves to define U_e. Conversely, U_h, which represents the external potential of photoexcited holes in water oxidation, is characterized by the energy differential between the VBM of the $MoSi_2P_4$ layer and the hydrogen reduction potential.[49] It is found to be 1.537/1.509/1.480 V for the +1%/+3%/+5% biaxial tensile strain at pH = 0. The calculated values of U_h and U_e may generate adequate driving forces to facilitate both the oxygen evolution reaction (OER) and hydrogen evolution reaction (HER). Furthermore, this suggests that the photoexcited electrons on the GaN and photoexcited holes on the $MoSi_2P_4$ would preferentially migrate to react with water rather than with themselves, thus generating significant resistance to incident light-induced corrosion.[49,50] These results indicate that the hydrogen and oxygen evolution reaction can happen readily and be separated naturally from different layers. Thus, the strained GaN/$MoSi_2P_4$ heterobilayer can act as a direct Z-scheme high-efficiency photocatalyst for water splitting to H_2 and O_2.

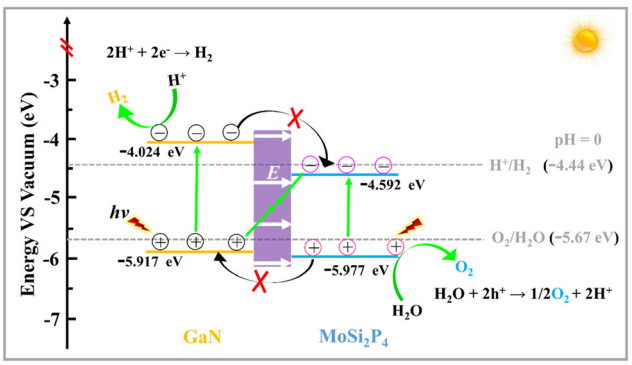

Fig. 6 Transfer processes of photogenerated electrons and holes in a direct Z-scheme AA5 GaN/$MoSi_2P_4$ heterobilayer at a biaxial tensile strain of +1%.

3.2 Overall water splitting

For observed AA5 GaN/$MoSi_2P_4$ heterobilayer under biaxial tensile strains of +1%–+5%, the first requisite for overall water splitting is acquired by their suitable band edge positions. Nevertheless, it remains unclear whether the photoexcited electrons and holes in the strained AA5 GaN/$MoSi_2P_4$ possess sufficient driving force to facilitate the overall water splitting process, specifically the OER and HER. To make it clear, we take AA5 GaN/$MoSi_2P_4$ under a biaxial tensile strain of +1%, for example, and explore the OER and HER mechanisms to confirm the photocatalytic activity.

The OER on the surface of the $MoSi_2P_4$ layer is first investigated by following the four-electron ($4e^-$) reaction pathway:

$$* + H_2O \rightarrow OH^* + H^+ + e^-, \quad (3)$$

$$OH^* \rightarrow O^* + H^+ + e^-, \quad (4)$$

$$O^* + H_2O \rightarrow O^*OH^* + H^+ + e^-, \quad (5)$$

$$O^*OH^* \rightarrow O^*O^* + H^+ + e^-, \quad (6)$$

$$O^*O^* \rightarrow O_2, \quad (7)$$

where "*" shows the active sites of the intermediates on the AA5 GaN/$MoSi_2P_4$ heterobilayer. The atomic configurations of intermediates along the water oxidation reaction pathway on the $MoSi_2P_4$ layer under conditions of pH = 0 and absence of light irradiation (U_h = 0) are illustrated in Fig. 7a. Correspondingly, Fig. 7b illustrates the associated free energy profile for this process. In the initial stage of water oxidation, the water molecule undergoes conversion to an OH* species ($H_2O + * \rightarrow OH^* + H^+ + e^-$), which adsorbs onto the surface of the P site with a Gibbs free energy change ΔG of 1.422 eV. Second, the OH* undergoes oxidation to form an oxygen radical (O*), releasing a proton and an electron in the process ($OH^* \rightarrow O^* + H^+ + e^-$), which is an exothermic process that releases 0.671 eV in the free-energy profile, suggesting a spontaneous process. During the third phase, the O* species undergoes a reaction with an additional water molecule, forming an O*OH* species. This process has a ΔG of 1.250 eV ($O^* + H_2O \rightarrow O^*OH^* + H^+ + e^-$), which is less than the ΔG of the first step. In the final step, the O*OH* species undergoes a process in which it releases an electron and a proton, resulting in the formation of an O_2 molecule ($O^*OH^* \rightarrow H^+ + e^- + O_2$), being endothermic for the step by 2.885 eV. In fact, the water oxidation half reaction proves energetically unfavorable on the $MoSi_2P_4$ layer surface when no light irradiation is present. Converting O*O* to O_2 represents the rate-limiting step, exhibiting a limiting potential (U_{lim}) of −3.104 V. Therefore, to facilitate the entire reaction at pH = 0, the $MoSi_2P_4$ layer necessitates an external voltage of 3.104 V. Upon light irradiation, photogenerated holes in the 1% strained GaN/$MoSi_2P_4$ can only provide an external potential U_h of 1.537 V for water oxidation, which cannot proceed spontaneously with the reaction. Nevertheless, the external potential can cause all four fundamental steps to become energetically favorable in the free-energy landscape after adjusting the energy of these charge-related processes by $-eU_h$. This suggests that the $MoSi_2P_4$ layer can advance water oxidation at pH = 0 under light irradiation.

Unlike water oxidation, the active site for the HER is the N site of the GaN layer. The distinct active sites for the two half reactions can markedly enhance the efficiency of photocatalytic processes. In the absence of light stimulation (U = 0), the GaN layer shows a thermodynamically favorable ΔG of −0.679 eV for the production of H* species, following the reaction pathway: $* + H^+ + e^- \rightarrow H^*$, suggesting an exothermic process that can proceed spontaneously under dark conditions. The process of creating H_2 from H* species is endothermic at pH = 0 ($H^* + H^+ + e^- \rightarrow H_2 + *$), as shown in Fig. 6d. Under an external potential

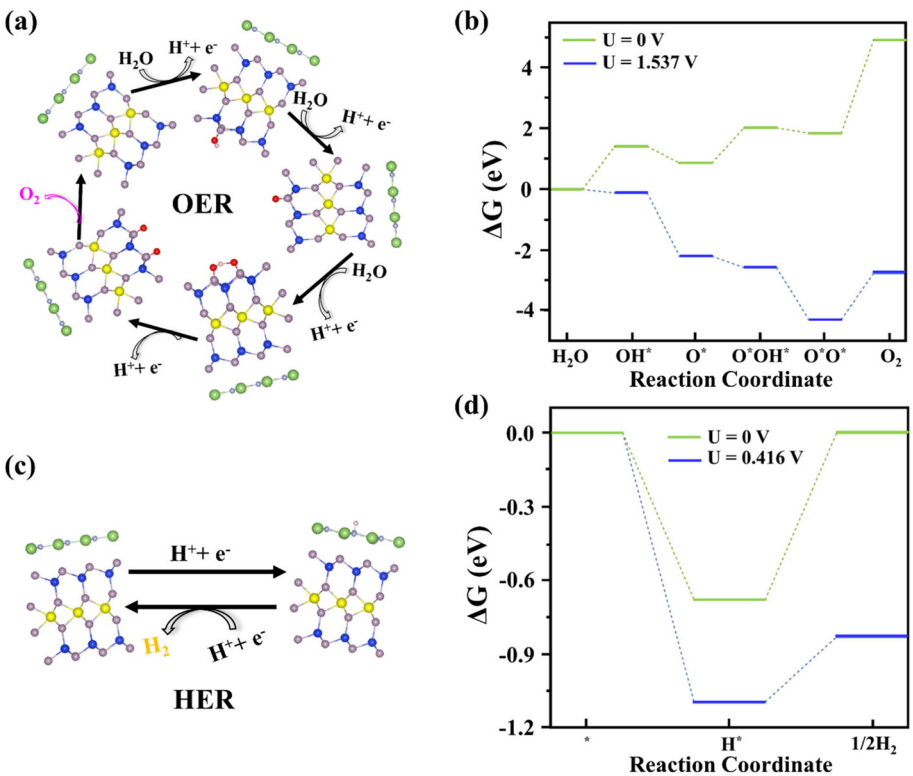

Fig. 7 (a and c) Schematics for the overall water-splitting reactions (OER and HER) on a +1% strained AA5 GaN/$MoSi_2P_4$ heterobilayer. O and H atoms are marked by red and light pink balls, respectively. (b and d) Energy diagrams depicting the free energy profiles for the $4e^-$ OER and $2e^-$ HER pathways in the +1% strained AA5 GaN/$MoSi_2P_4$ heterobilayer at pH = 0 without and with light irradiation.

U_e of 0.416 V provided by the photogenerated electrons of the heterobilayer, the free-energy profile for the hydrogen reduction reaction exhibits a downhill trajectory for both elementary steps. Consequently, the +1% strained GaN/$MoSi_2P_4$ heterobilayer can efficiently split pure water when exposed to light, as both OER and HER can proceed.

3.3 Optical properties

An efficient photocatalyst should possess a strong light-harvesting performance for the incident sunlight, especially the infrared and visible lights (accounting for ~93% of the sunlight). The optical properties of 2D materials are significantly influenced by electron–hole couplings primarily due to the substantial effects of excitons. To elucidate the light-harvesting efficacy, an analysis of the optical characteristics of the AA5 GaN/$MoSi_2P_4$ heterobilayer is conducted under different biaxial tensile strains (0, +1%, +3%, and +5%) by applying the state-of-the-art G_0W_0+BSE method. Fig. 8a depicts the imaginary component $\varepsilon_2(\omega)$ of frequency-dependent dielectric function $\varepsilon(\omega)$ of the pristine AA5 GaN/$MoSi_2P_4$, where the G_0W_0+BSE (G_0W_0+RPA) curve corresponds to an optical absorption spectrum, including (excluding) the photogenerated e–h couplings. Compared with the G_0W_0+RPA profile, the G_0W_0+BSE profile is largely red-shifted due to the outstanding e–h couplings, in which a large number of exciton states with large oscillator strengths are observed in the energy region of 0.5–3.16 eV. In particular, two bright bound exciton states below the QP bandgap (1.479 eV) are located at 0.951 and 1.282 eV (as shown in the orange arrows in Fig. 8a). For a direct semiconductor, the first bright exciton state is very important and can be captured by experimental observation. By analysing the oscillator strength, the first bright bound exciton state is from the VBM → CBM vertical transition at the K-point (Fig. 4b). Thus, the excitation energy of 0.951 eV is regarded as the optical gap of pristine AA5 GaN/$MoSi_2P_4$, which can be compared with the experimentally measured gap. Further, the binding energy ($E_{b\text{-exciton}}$) of the first bright bound exciton is estimated to be 0.528 eV by the difference between the QP bandgap ($E_{g\text{-QP}}$) and excitation energy (E_e), *i.e.* $E_{b\text{-exciton}} = E_{g\text{-QP}} - E_e$, which can resist thermal fluctuation at room temperature. The calculated exciton binding energy of pristine AA5 GaN/$MoSi_2P_4$ is compared to those of other 2D materials.[49,51]

Fig. 8b shows the strain-dependent optical absorptions of AA5 GaN/$MoSi_2P_4$, in which the $\varepsilon_2(\omega)$ is observed at the strains of δ = +1%, +3%, +5%. The focused first absorption peak is significantly red-shifted by about 0.463 eV from 0.951 eV (δ = 0) to 0.492 eV (δ = +5%). The first absorption peaks of the strained systems are also examined and verified to be from the VBM → CBM vertical transitions at the K-point. The estimated $E_{b\text{-exciton}}$ corresponding to the first absorption peaks is changed from 528 meV from δ = 0 to 259 meV for δ = +5%, as listed in Table 1, indicating that the binding energy of exciton in the AA5 GaN/$MoSi_2P_4$ can be tuned significantly by the applied biaxial strains. Smaller $E_{b\text{-exciton}}$ can result in the photogenerated electron around the hole delocalized in a larger space, thus making the photogenerated e–h pair recombination difficult. In addition, compared with that at δ = 0, the optical absorption of AA5 GaN/$MoSi_2P_4$ under the biaxial tensile strain of +5% reveals a significant enhancement in the near-infrared and visible range. Consequently, the biaxial tensile strain in the AA5 GaN/$MoSi_2P_4$ heterobialyer can induce smaller exciton binding energy and enhance light absorption.

Table 1 Bandgaps of AA5 GaN/$MoSi_2P_4$ at biaxial strains of δ = 0, +1%, +3%, +5% from the PBE ($E_{g\text{-PBE}}$) and G_0W_0 ($E_{g\text{-QP}}$) levels. The obtained excitation and exciton binding energies (E_e and $E_{b\text{-exciton}}$) correspond to the first absorption peak. The energy unit is adopted to be "eV"

δ	$E_{g\text{-PBE}}$	$E_{g\text{-QP}}$	E_e	$E_{b\text{-exciton}}$
0	0.825	1.479	0.951	0.528
+1%	0.688	1.325	0.810	0.515
+3%	0.350	1.024	0.644	0.380
+5%	0.101	0.751	0.492	0.259

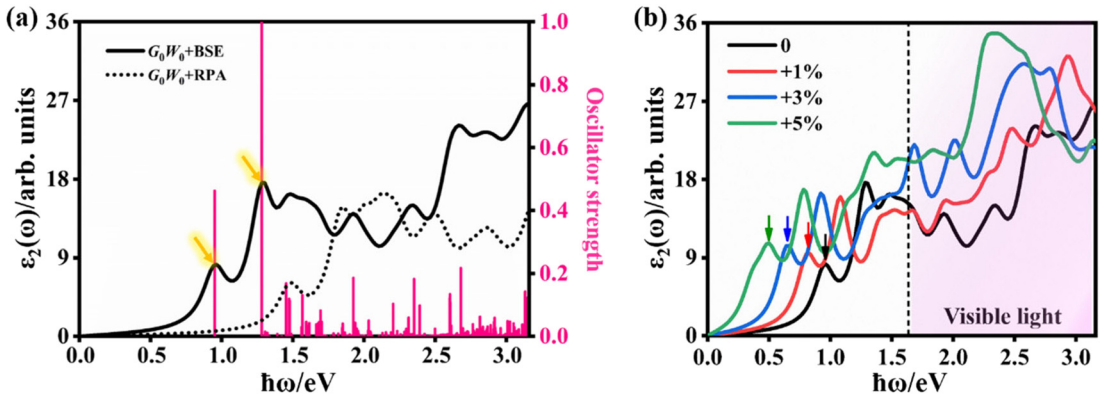

Fig. 8 (a) Imaginary part (ε_2) of the dielectric function of the pristine AA5 GaN/$MoSi_2P_4$ heterobilayer is calculated with (black solid line) and without (black short dash line) electron–hole coupling included, *i.e.*, G_0W_0+BSE and G_0W_0+RPA, respectively. (b) ε_2 of the GaN/$MoSi_2P_4$ heterobilayer at biaxial tensile strains of +1%, +3%, and +5% using the G_0W_0+BSE method. The incident polarized light is along the *x* direction. A Lorentzian broadening of 100 meV is applied in these calculations.

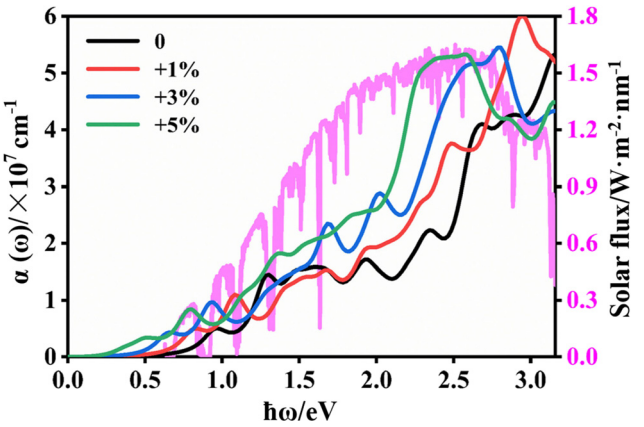

Fig. 9 Light absorption coefficients of the AA5 GaN/$MoSi_2P_4$ heterobilayer at different biaxial strains, which are from the G_0W_0+BSE level. Solar irradiance at an air mass of 1.5G is utilized for comparison.

Finally, to further measure the light harvesting ability of the AA5 GaN/$MoSi_2P_4$ heterobilayer for the sunlight, we calculated its light absorption coefficient $\alpha(\omega)$ by applying the following equation:[52,53]

$$\alpha(\omega) = \frac{\sqrt{2}\omega}{c}[\sqrt{\varepsilon_1{}^2(\omega) + \varepsilon_2{}^2(\omega)} - \varepsilon_1(\omega)]^{\frac{1}{2}}, \quad (8)$$

where $\varepsilon_1(\omega)$ is the real part of the $\varepsilon(\omega)$. As shown in Fig. 9, the absorption intensity can achieve 10^6 cm^{-1} in the observed wide energy range, indicating that AA5 GaN/$MoSi_2P_4$ is very active in the visible and near-infrared parts of the sunlight. In particular, the absorption intensities can achieve a maximum value of about 5.0×10^7 cm^{-1} at a phonon energy of 3.160 eV. In addition, with the increased tensile strain, the light absorption coefficient is improved significantly. Consequently, the strained AA5 GaN/$MoSi_2P_4$ heterobilayer demonstrates efficient harvesting of incident sunlight, which may enhance its potential application as a water splitting photocatalyst.

4 Conclusions

In summary, by employing DFT+G_0W_0+BSE calculations, this study systematically investigates the structural, electronic, photocatalytic, and optical properties of a new GaN/$MoSi_2P_4$ van der Waals heterobilayer. The dynamical, energetic, and thermodynamic stabilities are verified by the phonon spectrum, binding energy, and AIMD. The GaN/$MoSi_2P_4$ with type-I band alignment is predicted to have a direct quasi-particle bandgap of 1.479 eV at the G_0W_0 level. It also exhibits a strong absorption coefficient of more than 10^6 cm^{-1} for visible and near-infrared lights. The calculated binding energy of exciton in the GaN/$MoSi_2P_4$ is 528 meV, which can withstand thermal fluctuation at room temperature. More interestingly, a +1% biaxial tensile strain can transform the GaN/$MoSi_2P_4$ from type-I to type-II. The type-II nature in the strained GaN/$MoSi_2P_4$ can facilitate the effective separation of photogenerated electron–hole pairs. The observed built-in electric field oriented from the GaN layer to the $MoSi_2P_4$ layer further indicates that it constitutes a direct Z-scheme heterostructure. The formed Z-scheme can greatly optimize the redox ability. Additionally, the distinct layers of GaN/$MoSi_2P_4$ facilitate both water oxidation and hydrogen reduction half-reactions, which are driven by the potentials generated from photoexcited electrons and holes. With the increase in applied biaxial tensile strain, the quasi-particle bandgap is significantly reduced to 0.751 eV (+5%) and significantly enhanced absorptions for the visible and near-infrared lights are observed. These tunable properties in the GaN/$MoSi_2P_4$ vdWs heterobilayer can endow it as a potential material for optoelectronic and photocatalytic water splitting devices.

Data availability

The data supporting this work are available from the corresponding author upon reasonable request.

Conflicts of interest

There are no conflicts to declare.

Acknowledgements

This work was supported by the foundations from Jiangsu University of Science and Technology (No. 1052931610), Natural Science Foundation of Jiangsu Province of China (BK20220407), Natural Science Foundation of China (No. 12404273), and China Postdoctoral Fund Project (2024M750835, 2024T170251).

References

1 X. Li, L. Tao, Z. Chen, H. Fang, X. Li, X. Wang, J.-B. Xu and H. Zhu, *Appl. Phys. Rev.*, 2017, **4**, 021306.
2 C. Chang, W. Chen, Y. Chen, Y. Chen, Y. Chen, F. Ding, C. Fan, H. Jin Fan, Z. Fan, C. Gong, Y. Gong, Q. He, X. Hong, S. Hu, W. Hu, W. Huang, Y. Huang, W. Ji, D. Li, L.-J. Li, Q. Li, L. Lin, C. Ling, M. Liu, N. Liu, Z. Liu, K. Ping Loh, J. Ma, F. Miao, H. Peng, M. Shao, L. Song, S. Su, S. Sun, C. Tan, Z. Tang, D. Wang, H. Wang, J. Wang, X. Wang, X. Wang, A. T. S. Wee, Z. Wei, Y. Wu, Z.-S. Wu, J. Xiong, Q. Xiong, W. Xu, P. Yin, H. Zeng, Z. Zeng, T. Zhai, H. Zhang, H. Zhang, Q. Zhang, T. Zhang, X. Zhang, L.-D. Zhao, M. Zhao, W. Zhao, Y. Zhao, K.-G. Zhou, X. Zhou, Y. Zhou, H. Zhu, H. Zhang and Z. Liu, *Acta Phys.-Chim. Sin.*, 2021, **37**, 2108017.
3 Y. Yin, Q. Gong, M. Yi and W. Guo, *Adv. Funct. Mater.*, 2023, **33**, 2214050.
4 B. Cho, J. Yoon, S. K. Lim, A. R. Kim, D.-H. Kim, S.-G. Park, J.-D. Kwon, Y.-J. Lee, K.-H. Lee, B. H. Lee, H. C. Ko and M. G. Hahm, *ACS Appl. Mater. Interfaces*, 2015, **7**, 16775–16780.

5 N. Zhang, A. Surrente, M. Baranowski, D. K. Maude, P. Gant, A. Castellanos-Gomez and P. Plochocka, *Nano Lett.*, 2018, **18**, 7651–7657.
6 B. Du, Y. Li, M. Jiang, H. Zhang, L. Wu, W. Wen, Z. Liu, Z. Fang and T. Yu, *Nano Lett.*, 2022, **22**, 1649–1655.
7 M. Yankowitz, Q. Ma, P. Jarillo-Herrero and B. J. LeRoy, *Nat. Rev. Phys.*, 2019, **1**, 112–125.
8 H. Wang, Z. Li, D. Li, P. Chen, L. Pi, X. Zhou and T. Zhai, *Adv. Funct. Mater.*, 2021, **31**, 2103106.
9 E. Barré, M. Dandu, S. Kundu, A. Sood, F. H. da Jornada and A. Raja, *Nat. Rev. Mater.*, 2024, **9**, 499–508.
10 R. Zhang, L. Zhang, Q. Zheng, P. Gao, J. Zhao and J. Yang, *J. Phys. Chem. Lett.*, 2018, **9**, 5419–5424.
11 Y.-L. Hong, Z. Liu, L. Wang, T. Zhou, W. Ma, C. Xu, S. Feng, L. Chen, M.-L. Chen, D.-M. Sun, X.-Q. Chen, H.-M. Cheng and W. Ren, *Science*, 2020, **369**, 670–674.
12 H. Yao, C. Zhang, Q. Wang, J. Li, Y. Yu, F. Xu, B. Wang and Y. Wei, *Nanomaterials*, 2021, **11**, 559.
13 X. Liu, H. Zhang, Z. Yang, Z. Zhang, X. Fan and H. Liu, *Phys. Lett. A*, 2021, **420**, 127751.
14 Q. H. Wang, K. Kalantar-Zadeh, A. Kis, J. N. Coleman and M. S. Strano, *Nat. Nanotechnol.*, 2012, **7**, 699–712.
15 Y. Wang and Y. Ding, *Appl. Phys. Lett.*, 2022, **121**, 073101.
16 T. K. Sahu, S. P. Sahu, K. P. S. S. Hembram, J.-K. Lee, V. Biju and P. Kumar, *NPG Asia Mater.*, 2023, **15**, 49.
17 Z. Y. Al Balushi, K. Wang, R. K. Ghosh, R. A. Vilá, S. M. Eichfeld, J. D. Caldwell, X. Qin, Y.-C. Lin, P. A. DeSario, G. Stone, S. Subramanian, D. F. Paul, R. M. Wallace, S. Datta, J. M. Redwing and J. A. Robinson, *Nat. Mater.*, 2016, **15**, 1166.
18 H. Shu, X. Niu, X. Ding and Y. Wang, *Appl. Surf. Sci.*, 2019, **479**, 475–481.
19 W.-J. Yin, X.-L. Zeng, B. Wen, Q.-X. Ge, Y. Xu, G. Teobaldi and L.-M. Liu, *Front. Phys.*, 2020, **16**, 33501.
20 J. Wang, H. Shu, P. Liang, N. Wang, D. Cao and X. Chen, *J. Phys. Chem. C*, 2019, **123**, 3861–3867.
21 Z. Cui, K. Ren, Y. Zhao, X. Wang, H. Shu, J. Yu, W. Tang and M. Sun, *Appl. Surf. Sci.*, 2019, **492**, 513–519.
22 N. B. Singh, R. Mondal, J. Deb, D. Paul and U. Sarkar, *ACS Appl. Nano Mater.*, 2024, **7**, 6704–6711.
23 P. Giannozzi, S. Baroni, N. Bonini, M. Calandra, R. Car, C. Cavazzoni, D. Ceresoli, G. L. Chiarotti, M. Cococcioni, I. Dabo, A. Dal Corso, S. de Gironcoli, S. Fabris, G. Fratesi, R. Gebauer, U. Gerstmann, C. Gougoussis, A. Kokalj, M. Lazzeri, L. Martin-Samos, N. Marzari, F. Mauri, R. Mazzarello, S. Paolini, A. Pasquarello, L. Paulatto, C. Sbraccia, S. Scandolo, G. Sclauzero, A. P. Seitsonen, A. Smogunov, P. Umari and R. M. Wentzcovitch, *J. Phys.: Condens. Matter*, 2009, **21**, 395502.
24 J. P. Perdew, K. Burke and M. Ernzerhof, *Phys. Rev. Lett.*, 1996, **77**, 3865–3868.
25 G. Román-Pérez and J. M. Soler, *Phys. Rev. Lett.*, 2009, **103**, 096102.
26 S. Baroni, S. de Gironcoli, A. Dal Corso and P. Giannozzi, *Rev. Mod. Phys.*, 2001, **73**, 515–562.
27 J. K. Nørskov, J. Rossmeisl, A. Logadottir, L. Lindqvist, J. R. Kitchin, T. Bligaard and H. Jónsson, *J. Phys. Chem. B*, 2004, **108**, 17886–17892.
28 Á. Valdés, Z.-W. Qu, G.-J. Kroes, J. Rossmeisl and J. K. Nørskov, *J. Phys. Chem. C*, 2008, **112**, 9872–9879.
29 NIST Computational Chemistry Comparison and Benchmark Database, 2018, vol. NIST Standard Reference Database Number 101, Release 19, edited by Russell D. Johnson III, available at **https://cccbdb.nist.gov/**.
30 R. W. Godby and R. J. Needs, *Phys. Rev. Lett.*, 1989, **62**, 1169.
31 A. Oschlies, R. W. Godby and R. J. Needs, *Phys. Rev. B: Condens. Matter Mater. Phys.*, 1995, **51**, 1527.
32 E. E. Salpeter and H. A. Bethe, *Phys. Rev.*, 1951, **84**, 1232.
33 G. Onida, L. Reining and A. Rubio, *Rev. Mod. Phys.*, 2002, **74**, 601–659.
34 L. Yang, C. D. Spataru, S. G. Louie and M. Y. Chou, *Phys. Rev. B: Condens. Matter Mater. Phys.*, 2007, **75**, 201304.
35 A. Marini, C. Hogan, M. Grüning and D. Varsano, *Comput. Phys. Commun.*, 2009, **180**, 1392–1403.
36 H. Şahin, S. Cahangirov, M. Topsakal, E. Bekaroglu, E. Akturk, R. T. Senger and S. Ciraci, *Phys. Rev. B: Condens. Matter Mater. Phys.*, 2009, **80**, 155453.
37 B. Mortazavi, B. Javvaji, F. Shojaei, T. Rabczuk, A. V. Shapeev and X. Zhuang, *Nano Energy*, 2021, **82**, 105716.
38 Y. Guo, J. Min, X. Cai, L. Zhang, C. Liu and Y. Jia, *J. Phys. Chem. C*, 2022, **126**, 4677–4683.
39 M. Sun, M. Re Fiorentin, U. Schwingenschlögl and M. Palummo, *npj 2D Mater. Appl.*, 2022, **6**, 81.
40 A. Onen, D. Kecik, E. Durgun and S. Ciraci, *Phys. Rev. B*, 2016, **93**, 085431.
41 X. Wang, W. Ju, D. Wang, X. Li and J. Wan, *Phys. Chem. Chem. Phys.*, 2023, **25**, 18247–18258.
42 T. Björkman, A. Gulans, A. V. Krasheninnikov and R. M. Nieminen, *Phys. Rev. Lett.*, 2012, **108**, 235502.
43 A. Ramasubramaniam, *Phys. Rev. B: Condens. Matter Mater. Phys.*, 2012, **86**, 115409.
44 K. F. Mak, C. Lee, J. Hone, J. Shan and T. F. Heinz, *Phys. Rev. Lett.*, 2010, **105**, 136805.
45 M. Pandey, C. Pandey, R. Ahuja and R. Kumar, *Nano Energy*, 2023, **109**, 108278.
46 S. Yang, Y. Chen and C. Jiang, *InfoMat*, 2021, **3**, 397–420.
47 V. Chakrapani, J. C. Angus, A. B. Anderson, S. D. Wolter, B. R. Stoner and G. U. Sumanasekera, *Science*, 2007, **318**, 1424–1430.
48 Y. Xu and M. A. A. Schoonen, *Am. Mineral.*, 2000, **85**, 543–556.
49 M. Qiao, J. Liu, Y. Wang, Y. Li and Z. Chen, *J. Am. Chem. Soc.*, 2018, **140**, 12256–12262.
50 S. Chen and L.-W. Wang, *Chem. Mater.*, 2012, **24**, 3659–3666.
51 H. Seksaria, A. Kishore and A. De Sarkar, *Phys. Chem. Chem. Phys.*, 2024, **26**, 22882–22893.
52 F. Karlický and J. Turoň, *Carbon*, 2018, **135**, 134–144.
53 X. Liu, P. Gao, W. Hu and J. Yang, *J. Phys. Chem. Lett.*, 2020, **11**, 4070–4079.